Author/s:
Hu, Y;Li, J;Ju, Y;Houston, ZH;Fletcher, NL;De Rose, R;Fernandes, S;Hagemeyer, CE;Alt, K;Thurecht, KJ;Cortez-Jugo, C;Caruso, F

Title:
Template-Assisted Antibody Assembly: A Versatile Approach for Engineering Functional Antibody Nanoparticles

Date:
2022-04-26

Citation:
Hu, Y., Li, J., Ju, Y., Houston, Z. H., Fletcher, N. L., De Rose, R., Fernandes, S., Hagemeyer, C. E., Alt, K., Thurecht, K. J., Cortez-Jugo, C. & Caruso, F. (2022). Template-Assisted Antibody Assembly: A Versatile Approach for Engineering Functional Antibody Nanoparticles. Chemistry of Materials, 34 (8), pp.3694-3704. https://doi.org/10.1021/acs.chemmater.1c04397.

Template-Assisted Antibody Assembly: A Versatile Approach for Engineering Functional Antibody Nanoparticles

Yingjie Hu,[a] Jianhua Li,[a] Yi Ju,[a] Zachary H. Houston,[b] Nicholas L. Fletcher,[b] Robert De Rose,[a] Soraia Fernandes,[a,c] Christoph E. Hagemeyer,[d] Karen Alt,[d] Kristofer J. Thurecht,[b] Christina Cortez-Jugo,[a] and Frank Caruso[,a]*

[a] ARC Centre of Excellence in Convergent Bio-Nano Science and Technology, and the Department of Chemical Engineering, The University of Melbourne, Parkville, Victoria 3010, Australia

[b] ARC Centre of Excellence in Convergent Bio-Nano Science and Technology, and the Centre for Advanced Imaging, The University of Queensland, St Lucia, Queensland 4072, Australia

[c] International Clinical Research Centre (ICRC), St. Anne's University Hospital, CZ-65691 Brno, Czech Republic

[d] Australian Centre for Blood Diseases, Central Clinical School, Monash University, Melbourne, Victoria 3004, Australia

*Corresponding author. E-mail: fcaruso@unimelb.edu.au

ABSTRACT

The clinical success of monoclonal antibody therapy has inspired research in understanding the fundamental molecular basis of antibody–antigen interactions and the engineering of antibodies and antibody assemblies with enhanced or novel properties. In particular, colloidally stable antibody assemblies can enhance dosing strategies and enable combined therapy of a mixture of antibodies or biologics. Herein, nano-assemblies of therapeutic antibodies were fabricated with controlled physicochemical properties using a versatile template-mediated assembly method. The antibody nanoparticles (AbNPs), cross-linked with poly(ethylene glycol)-*N*-hydroxysuccinimide, were monodisperse, with particle diameters consistent with the template size (250 nm). When assembled using Herceptin or Kadcyla as a model antibody and antibody–drug conjugate, respectively, the nanoparticles retained the selectivity of the monoclonal antibody and recognized >98% of cells expressing the target receptors on cell membranes. Unlike the free Herceptin antibody, which was predominantly localized at the surface, the AbNPs were internalized via receptor-mediated endocytosis, presenting opportunities for delivering monoclonal antibodies intracellularly at high concentrations and/or against intracellular targets. With the vast array of antibodies that could be applied and different cross-linking chemistries possible, the reported antibody assembly strategy provides a versatile platform for the development of antibody assemblies for therapeutic, diagnostic, and clinical applications.

INTRODUCTION

Monoclonal antibodies are the fastest growing class of therapeutics and have a proven clinical track record for the treatment and diagnosis of several diseases, including cancer and inflammatory conditions, owing to their high specificity and efficacy.[1–3] For cellular targets, antibodies bind to

their specific antigen, for example receptors present on the cellular membrane that trigger a cascade of intracellular signaling events or intracellular targets that influence various cellular activities.[4,5] Many monoclonal antibodies, approved by the Food and Drug Administration (FDA), and their drug conjugates, bind to specific receptors overexpressed on tumor cells, enabling the delivery of the antibody, as well as therapeutic or imaging agents to tumors.[6] Given their significance in medical research and for clinical use, it is important to understand the fundamental molecular basis of antibody–antigen interactions, explore new antibody targets, and design antibodies with improved functions.

Antibodies have been widely applied as targeting ligands in nanotechnology-enabled therapeutic modalities, including liposomes,[7] protein nanoparticles,[8] and polymeric micelles,[9] for drug delivery and imaging applications. The attachment of antibodies to these nanoscale platforms has been typically achieved through surface assembly of the antibody molecules using covalent or noncovalent bioconjugation techniques.[10,11] The physicochemical properties of the underlying substrate, including material type, size, and shape,[10,12–14] have been shown to influence the interactions of the immobilized antibodies with their targets. However, little is known about the effect of assembled antibodies or antibody clusters themselves on antibody–antigen interactions, mainly because of the challenge in preparing "pure" antibody nanoparticles with controlled size despite limited attempts made to fabricate antibody nano-assemblies via self-assembly methods including copolymer conjugation and antibody complexation with catechin derivatives.[15,16] These clusters are a separate class to undefined antibody aggregates of heterogeneous size that are formed during the manufacture of monoclonal antibodies.[17,18] The formulation of nonimmunogenic antibody clusters of homogeneous, submicrometer size and composition could potentially offer

further applications for antibody therapeutics and improved therapeutic outcomes over free antibodies.

Pure protein particles (diameter of 930 nm) have previously been prepared by a template-mediated method using sacrificial mesoporous silica (MS) particles.[19] In contrast, the template-mediated synthesis of smaller pure protein particles has remained a challenge partly because of the need for sacrificial templates with large pore sizes, to accommodate proteins, and with interconnecting pores to enable cross-linking. Particle size influences the ability of a particle to cross biological barriers, including cell entry, and is an important criterion to reducing the immunogenicity of antibody-based therapeutics.[17,18] Recently, a method for preparing 200 nm MS particles with large dendritic pores was reported[20–22] that could allow the infiltration of larger proteins, including whole monoclonal antibodies, which have a typical molecular weight (M_w) of ~150 kDa. Herein, we exploit the large pore size of these MS particles and employ a simple template-mediated approach to fabricate amide-stabilized antibody nanoparticles with controlled physicochemical properties. The versatility of the approach is demonstrated using the therapeutic antibody Herceptin and its drug conjugate Kadcyla. We evaluate how these nano-assembled antibody nanoparticles (AbNPs) interact with targeted receptors and their potential effects on cellular activities and investigate their biodistribution in vivo, including tumor targeting capacity.

EXPERIMENTAL SECTION

Materials. Cetyltrimethylammonium bromide (CTAB), tetraethyl orthosilicate (TEOS), triethanolamine (TEA), sodium salicylate (NaSal), hydrogen chloride (HCl), hydrofluoric acid (HF, 48 wt%), ammonium fluoride (NH_4F), sodium carbonate (Na_2CO_3), dimethyl sulfoxide (DMSO), phenazine methosulfate (PMS), collagen (type 1 from rat tail), and immunoglobulin G (IgG) from sheep serum were purchased from Sigma-Aldrich. Methanol was purchased from

ChemSupply Australia. Poly(ethylene glycol)-*N*-hydroxysuccinimide (PEG-NHS, M_w 600) was purchased from Creative PEGworks. Pierce BCA protein assay kit, Alexa Fluor 488 carboxylic acid succinimidyl ester (AF488), Alexa Fluor 647 carboxylic acid succinimidyl ester (AF647), RPMI 1640 medium (GlutaMAX Supplement), Dulbecco's modified Eagle's medium (DMEM; with 4.5 g L^{-1} glucose, with L-glutamine), fetal bovine serum (FBS), Dulbecco's phosphate-buffered saline (DPBS) buffer, ErbB2 monoclonal antibody, Alexa Fluor 594-conjugated rabbit anti-mouse IgG (H+L) Superclonal secondary antibody, Alexa Fluor 594-wheat germ agglutinin conjugate (AF594-WGA), trihydrochloride (Hoechst 33342), and 2,3-bis[2-methoxy-4-nitro-5-sulfophenyl]-2*H*-tetrazolium-5-carboxanilide inner salt (XTT) were purchased from Thermo Fisher Scientific. Herceptin and Kadcyla antibodies were from Genentech/F. Hoffmann-La Roche Ltd. Thulium(III) *S*-2-(4-isothiocyanatobenzyl)-1,4,7,10-tetraazacyclododecane-1,4,7,10-tetraacetic acid (Tm-*p*-SCN-Bn-DOTA) and *p*-SCN-Bn-Deferoxamine (DFO) were purchased from Macrocyclics. Nitric acid (HNO_3; 60%) was purchased from Merck. Ultrapure water with a resistance of greater than 18 MΩ cm (Milli-Q water) was obtained from a three-stage Millipore Milli-Q Plus 185 purification system.

Preparation of AbNPs. MS templates with large pores were synthesized via the anion-assisted method using CTAB as a cationic surfactant, NaSal as a structure-directing agent, TEOS as a silica source, and TEA as a catalyst.[20–22] Briefly, 68 mg TEA, 380 mg CTAB, and 168 mg NaSal were successively added to 25 mL Milli-Q water, and the mixture was stirred at 80 °C in an oil bath for 1 h. Afterwards, 4 mL TEOS was slowly added to the above solution and stirred at 80 °C for 2 h. The products were collected by centrifugation at 10000*g* and washed three times with ethanol. The products were then purified by extraction with ~1 M HCl in methanol at 60 °C for 6 h; the

extraction process was repeated three times. The MS particles were washed with ethanol and finally oven-dried at 80 °C overnight.

Subsequently, 500 μL of IgG solution (2 mg mL^{-1}) was added to 500 μL of MS solution (2 mg mL^{-1}) in sodium acetate buffer (0.1 M, pH 5.0). The particle/protein dispersion was incubated for 2 h at room temperature on an Eppendorf thermomixer to allow the IgG molecules to infiltrate the pores of the template via electrostatic adsorption. Excess IgG was removed by centrifugation (~5000*g*, 5 min, ×3), and the IgG-loaded nanoparticles were dispersed in DPBS (pH 7.4). The loading capacity was determined by measuring the protein concentration before and after protein incubation with the MS template using a Pierce BCA protein assay kit according to the manufacturer's protocol. Cross-linking of the IgG molecules within the MS template was achieved by adding PEG-NHS cross-linker (50 μL of 20 mg mL^{-1} in DMSO) to the IgG-loaded MS in DPBS buffer, followed by incubation for 4 h at room temperature with constant agitation on a ThermoMixer. The AbNPs (IgGNPs in this case) were finally obtained by dissolving the MS template with 1 M HF/3 M NH_4F solution (pH ~5), followed by washing with DPBS buffer three times. *Caution! HF is highly toxic. Extreme care should be taken when handling HF solution, and only small quantities should be prepared.* Herceptin nanoparticles (HerNPs) and Kadcyla nanoparticles (KadNPs) were prepared using the same procedure.

Quantitative Analysis of Antibodies in AbNPs. The protein concentration of the AbNPs was determined using a Pierce BCA protein assay kit; particle concentration was measured by nanoparticle tracking analysis using a 405 nm laser. At a protein concentration of 0.02 mg mL^{-1}, the particle concentration is 2.23×10^9 particles mL^{-1} (Figure S2b). Thus, 1 mg of AbNPs (4.01×10^{15} IgG molecules) contains 1.12×10^{11} particles. Therefore, one AbNP contains approximately 3.58×10^4 IgG molecules ($4.01 \times 10^{15}/1.12 \times 10^{11}$).

Antibody Labeling. For the antibody labeling, 5 µL AF488 or AF647 (1 mg mL^{-1}) in DMSO was added to 200 µL of antibody solution (5 mg mL^{-1}) in DPBS buffer containing 0.1 M Na_2CO_3 (pH 8.3) for 2 h at room temperature (20 °C) with constant agitation. Excess free fluorophores were removed using Zeba spin desalting columns (40 kDa molecular weight cutoff, 2 mL). The labeled antibodies were then used to prepare AbNPs for imaging.

Particle Characterization. Transmission electron microscopy (TEM) images were taken on an FEI Tecnai Spirit microscope operating at 120 kV. Samples were prepared by placing a drop of a sample suspension (suspended in deionized water) on a carbon-coated copper grid and drying under ambient conditions. Particle concentration was determined by nanoparticle tracking using a Nanosight NS300 (Malvern Panalytical, UK). The surface area and porosity of the MS templates were determined from N_2 adsorption–desorption isotherms measured on an ASAP 2010 System (Micromeritics, USA). Hydrodynamic size distributions and zeta potentials were measured by dynamic light scattering (DLS) and microelectrophoresis, respectively, using a Zetasizer Nano ZS instrument (Malvern Instruments, UK). DLS measurements were performed in DPBS. Samples for zeta potential measurements were dispersed in 2 mM phosphate buffer (pH 7.4). Atomic force microscopy (AFM) images were acquired by a Cypher AFM (Asylum, USA). Circular dichroism (CD) spectra were recorded on a circular dichroism spectrometer (Model 401, AVIV Biomedical, USA). Fourier transform infrared (FTIR) spectra in attenuated total reflectance mode were recorded using an FTIR spectrometer (TENSOR II, Bruker, Germany).

Cell Culture. Human breast cancer BT-474 cells were maintained in RPMI medium 1640 supplemented with 10% (v/v) FBS. Human breast cancer MDA-MB-231 cells were incubated in DMEM with 10% (v/v) FBS. All cultures were maintained at 37 °C in a 5% CO_2-humidified atmosphere.

Cellular Association by Flow Cytometry. Cells were seeded at a density of 10^5 per well in 24-well plates and incubated at 37 °C overnight. Then, the culture medium was removed and replaced with fresh medium containing AF488-labeled free antibody and AbNPs (20 μg mL^{-1}). Cells were further incubated at 37 °C for 24 h. To assess receptor binding specificity, BT-474 were blocked by preincubating cells with nonfluorescent free Herceptin (20 μg mL^{-1}) at 37 °C for 3 h. After incubation, the media was replaced with fresh media containing the AF488-labeled AbNPs. Sample incubation was conducted under dynamic flow conditions using a self-contained device to maintain a well-mixed environment.[23] Subsequently, cells were gently washed with DPBS to remove unassociated nanoparticles, followed by treatment with 0.25% trypsin/ethylenediaminetetraacetic acid solution at 37 °C for 5 min. The cells were collected via centrifugation at 300*g* for 5 min and the resulting pellet was then resuspended in DPBS and analyzed by an Apogee A50-Micro flow cytometer. At least 10^4 cells were analyzed for each sample using the Apogee Histogram software v242. Graphs were created using FlowJo v10.5.

Cellular Internalization by Confocal Laser Scanning Microscopy (CLSM). Cells were seeded in an eight-well Lab-Tek II chambered slide at a density of 5×10^4 cells per well for 24 h. After incubation, cells were treated with AF488-labeled free antibody and AbNPs (20 μg mL^{-1}) for 24 h under dynamic flow conditions. Then, the cells were washed with DPBS, fixed with 4% paraformaldehyde for 10 min at room temperature (20 °C), stained with AF594-WGA for 5 min (optional), and counterstained with Hoechst 33342 for another 5 min. The cells were washed with DPBS after each staining step and finally immersed in DPBS before imaging, which was performed on a Nikon A1R+ confocal microscope.

For BT-474 cells, ErbB2 receptors were visualized by immunofluorescence staining. After treatment with free antibody and AbNPs, cells were fixed with 4% paraformaldehyde,

permeabilized with ice-cold ethanol for 10 min, and blocked with 2% bovine serum albumin (BSA) for 30 min. Then, cells were incubated with mouse anti-ErbB2 monoclonal antibody at a dilution of 1:100 (1 μg mL^{-1}) for 1 h at room temperature (20 °C) and further incubated with Alexa Fluor 594-conjugated rabbit anti-mouse IgG (H+L) Superclonal at a concentration of 1 μg mL^{-1} for 1 h. Washing with DPBS was performed between steps.

Internalization in Three-Dimensional (3D) Spheroids. To construct 3D spheroid models, BT-474 cells were seeded in a Perfecta3D hanging drop plate at a concentration of 1×10^4 cells per well in 40 μL of medium containing 0.075 mg mL^{-1} collagen. Cells were incubated for 24 h to allow the formation of spheroids in each droplet. Free antibody and AbNPs were gently added into the droplets at a concentration of 200 μg mL^{-1}. After incubation for 48 h, the spheroids were harvested from the plates, washed with DPBS, and then fixed with 4% paraformaldehyde for 20 min at room temperature (20 °C). After washing once with DPBS, the spheroids were stained with AF594-WGA and Hoechst 33342 for 1 h. Washing with DPBS was performed three times before final resuspension in DPBS for imaging on a Nikon A1R+ confocal microscope.

Cell Viability. Cells were seeded at a density of 1×10^4 cells per well in triplicate in 96-well microplates and allowed to adhere overnight. Free antibody and AbNPs were added and incubated with cells for 48 h under dynamic flow conditions. For all samples, the concentration of the antibody was kept constant at 20 μg mL^{-1}. After incubation, the culture medium was replaced with fresh medium containing 0.2 mg mL^{-1} of activated XTT (10 mL of 0.2 mg mL^{-1} XTT in complete medium was activated by adding 20 μL of 1 mM PMS in DPBS), and cells were allowed to incubate further at 37 °C for 3 h. Cell viability was measured on an Infinite M200 microplate reader (Tecan, Switzerland) at 475 nm, with 647 nm as the reference wavelength. Cell viability was expressed as a percentage by normalizing absorbance to untreated cells.

Biodistribution in Mice. Thulium (Tm)-labeled HerNPs were prepared by conjugating Tm-*p*-SCN-Bn-DOTA with the Herceptin antibodies. Briefly, 27.7 µL Tm-*p*-SCN-Bn-DOTA (10 mg mL^{-1}) in DMSO was added to 2 mL of antibody solution (5 mg mL^{-1}) in 0.1 M $NaHCO_3$ buffer (pH 9) for 2 h at 37 °C with constant agitation. Excess Tm-*p*-SCN-Bn-DOTA was removed using Zeba spin desalting columns (40 kDa molecular weight cutoff, 2 mL). The labeled antibodies were then used to prepare Tm-labeled HerNPs.

All biodistribution procedures were conducted in accordance with the Australian code for the care and use for scientific purpose, and experiments were approved by the University of Melbourne Animal Ethics Committee (10404). Mice were sourced from the Animal Resources Centre (Perth, Australia) and housed on a 12 h light/dark cycle with ad libitum access to food and water. Biodistribution of Tm-labeled HerNPs was studied in 6–7-week-old healthy female BALB/c mice. The mice were randomly divided into groups of 3 mice. A group of mice were injected intravenously with Tm-labeled HerNPs (1 mg mL^{-1}) or Tm-labeled free Herceptin antibody (1 mg mL^{-1}) at a dosage at 10 mg kg^{-1} via the lateral tail vein. A blood sample was drawn at 4 h after administration, and the mice were subsequently euthanized and perfused with DPBS. The organs of interest were harvested, weighed, and digested with 2 mL of 60% nitric acid at 70 °C for 2 h. *Caution! Extreme care should be taken when handling 60% nitric acid, which can only be used in a fume hood.* Tm signal in the blood and organ samples was measured by inductively coupled plasma mass spectrometry (ICP-MS). The signals measured from Tm-labeled HerNPs and free Herceptin at the administered dosage were used to calculate the percentage injected dose per gram (%ID g^{-1}) in each blood/organ sample.

Targeting in Tumor-Bearing Mice. *Preparation of DFO-AbNPs:* DFO-conjugated free antibody and AbNPs were prepared to allow for ^{89}Zr labeling. Briefly, 5 µL *p*-SCN-Bn-DFO (1

mg mL^{-1}) in DMSO solution was added to 1 mL of antibody solution (5 mg mL^{-1}) in 0.1 M $NaHCO_3$ buffer (pH 9), and the mixture was incubated for 1 h at 37 °C with constant agitation (400 rpm on a ThermoMixer). Excess *p*-SCN-Bn-DFO was removed using Zeba spin desalting columns (40 kDa molecular weight cutoff, 2 mL). The conjugated antibodies were then used to prepare DFO-conjugated AbNPs.

^{89}Zr Radiolabeling of DFO-AbNPs: The DFO-conjugated free antibodies (Herceptin, IgG) and AbNPs (HerNPs, IgGNPs) were incubated with ^{89}Zr (for imaging purposes) at molar ratios of 500:1 (DFO-conjugated free antibody:^{89}Zr) for Herceptin and IgG and 1000:1 (DFO-conjugated AbNP:^{89}Zr) for HerNPs and IgGNPs in 0.1 M pH 7.4 HEPES buffer for 45 min at 37 °C. Samples of each solution were taken and mixed 1:1 with 50 mM diethylenetriamine pentaacetate. Then, 5 µL of each solution was spotted on thin liquid chromatography (TLC) paper (Agilent iTLC-SG Glass microfiber chromatography paper impregnated with silica gel) and run with 50:50 H_2O:ethanol. Plates were then imaged on an Eckert & Ziegler Mini-Scan and Flow-Count iTLC Reader. Where necessary, unbound ^{89}Zr was removed by purification using 7 kDa molecular weight cutoff Zeba spin columns (Thermo Scientific) as per manufacturers protocols. All samples showed >90% ^{89}Zr radiolabeling.

Preparation of Subcutaneous Xenograft Tumor in Mice: All tumor targeting procedures were conducted in accordance with the Australian National Health and Medical Research Council's published Code of Practice for the Use of Animals in Research, and experiments were approved by the University of Queensland Animal Ethics Committee (AEC/AIBN/CAI/105/19). Mice were housed on a 12 h light/dark cycle with ad libitum access to food and water. Eight-week-old female BALB/c nu/nu mice were purchased from Animal Resources Centre (Perth, Australia). To establish BT-474 tumors for in vivo targeting experiments, immunocompromised mice were first

implanted subcutaneously with an estrogen hormone pellet at 9 weeks of age. The following day, 2.5×10^6 BT-474 cells in 50 µL of 50:50 PBS:Matrigel were injected subcutaneously in the right flank of each mouse. There was no evidence of ulceration at the time of dosing; the animals were closely monitored and remained in good condition apart from the growth of tumors. After 11 weeks of tumor growth (tumor weight up to ~0.4 g), ^{89}Zr-labeled free Herceptin, free IgG, HerNPs, and IgGNPs were injected via the tail vein (29G needle). Dosage was based on a radioactivity of 2.0 MBq for each sample.

Position Emission Tomography-Computed Tomography (PET-CT) Imaging of [^{89}Zr]Zr-AbNPs: Mice were anesthetized with isoflurane (IsoFlo, Abbott Laboratories) at a dose of 2% in a closed anesthetic induction chamber. Mice were monitored using ocular and pedal reflexes to ensure deep anesthesia. Once the mouse was deeply anesthetized, it was placed on an appropriate animal bed, where the anesthetic air mixture (1%) was delivered to its nose and mouth through a nose cone. Physiological monitoring (respiratory using a sensor probe) was achieved throughout all experiments using an animal monitoring system (BioVet™ system, m2m Imaging, Australia). Images were acquired using a Siemens Inveon PET-CT scanner following tail vein intravenous injection of the antibodies and particles.

The injection syringe was filled with the radioisotope solution (approximately 150 µL) and the activity in the syringe was measured using a dose calibrator (Capintec CRC-25) with a calibration factor of 35. The residual activity in the syringe after the tail vein injection was measured using the same dose calibrator, and the total volume injected in each mouse was calculated.

Calibration of the PET/CT scanner was performed with an in-house-manufactured phantom containing a known activity of ^{68}Ge solution as a radiation source.

The mice were positioned on the scanner bed (n = 3 per scan using a bed developed in-house) and micro-CT scans were acquired for anatomical co-registration. The CT images of the mice were acquired through an X-ray source with the voltage set to 80 kV and the current set to 500 µA. The scans were performed using 360° rotation with 120 rotation steps with a low magnification and a binning factor of four. The exposure time was 230 ms with an effective pixel size of 106 µm. The total CT scanning process took approximately 15 min. The CT images were reconstructed using Feldkamp reconstruction software (Siemens). Following CT imaging, PET scans were acquired at 4 h, 24 h, 48 h, and 5 days (120 h) after injection of the radiotracer, using 15–75 min static acquisitions. The PET images were reconstructed using an ordered-subset expectation maximization (OSEM2D) algorithm and analyzed using the Inveon Research Workplace software (IRW 4.1) (Siemens), which allows fusion of CT and PET images and definition of regions of interest (ROIs). CT and PET datasets of each individual animal were aligned using IRW software (Siemens) to ensure good overlap of the organs of interest. Three-dimensional ROIs were placed within the whole body, as well as all the organs of interest, such as the heart, kidney, lungs, bladder, liver, spleen, and tumors using morphologic CT information to delineate organs. Activity per voxel was converted to nci/cc using a conversion factor obtained by scanning a cylindrical phantom filled with a known activity of ^{89}Zr to account for PET scanner efficiency. Activity concentrations were then expressed as percentage of the decay-corrected injected activity per cm^3 of tissue that can be approximate as percentage injected dose per g (%ID g^{-1}).

Minimum Information Reporting in Bio–Nano Experimental Literature (MIRIBEL). The studies conducted herein, including material characterization, biological characterization, and experimental details, conform to the MIRIBEL reporting standard for bio–nano research,[24] and we include a companion checklist of these components in the Supporting Information.

RESULTS AND DISCUSSION

Synthesis and Characterization of AbNPs. The preparation of AbNPs is illustrated in Figure 1A. Antibodies (e.g., IgG) were loaded in MS templates, followed by cross-linking with PEG-NHS, which results in the formation of amide bonds with the amine groups on IgG. Removal of the MS templates results in AbNPs composed entirely of IgG and PEG. Here, AbNPs formed from a generic IgG (sheep IgG) are referred to as IgGNPs. Therapeutic monoclonal antibodies are of the IgG type, which are the most abundant type of antibody and have typical dimensions of approximately 14.5 nm × 8.5 nm × 4.0 nm.[25] To ensure a high loading of IgG in the templates, MS particles with large pore sizes that can accommodate IgGs were prepared.[20–22] High-resolution TEM revealed the porous and spherical morphology of the MS particles, with an average diameter of 250 nm (Figure 1B), as supported by DLS and nanoparticle tracking analyses (Figures 1D and S2a). The Brunauer–Emmett–Teller method and Barrett–Joyner–Halenda model were used to calculate the specific surface area and pore diameter distributions of the prepared MS, which were 624 $m^2\ g^{-1}$ and ~20 nm, respectively (Figure S1). The high porosity and large pore size of the MS particles are expected to afford a high IgG loading capacity, which is essential for ensuring that sufficient antigen or receptor binding sites are exposed and for efficient intracellular delivery. In physiological buffer (pH 7.4), the loading amount of sheep serum IgG (M_w ~150 kDa; Stokes radius (r_s) 6.4 nm; isoelectric point (pI) 6.1–8.5) into negatively charged (~ −28 mV) MS was as high as ~700 μg protein per 1 mg MS (loading efficiency of ~70%), which was significantly higher than the loading achieved with positively charged lysozyme (~380 μg protein per 1 mg MS; M_w 14.3 kDa; r_s 1.8 nm; pI 11) or negatively charged BSA (~320 μg protein per 1 mg MS; M_w 66.5 kDa; r_s 3.48 nm; pI 4.8) (Figure S3a) at the same feed protein concentration (1 mg mL^{-1}). The loading of IgG could be increased to ~900 μg protein per 1 mg of MS by incubating the templates

with IgG solution at a lower pH (sodium acetate buffer, pH 5) (data not shown). The results showed that the MS particles led to the highest loading of IgG molecules, which is mainly due to both the strong electrostatic interactions between the MS and IgG (Figure S3b) and the size-matching effect that allows the IgG molecules to be effectively entrapped within the pores of the templates (Figure S3c).

Freestanding AbNPs were obtained after the removal of the MS templates by HF treatment (pH ~5). IgG proteins are robust, and exposure of these antibodies to acidic pH induces minimal conformational changes, as reported elsewhere[26] and confirmed by the CD results—this is beneficial for retaining their bioactivity. TEM revealed that the resulting AbNPs had an average diameter of 250 nm (Figure 1C), which corresponds to the size of the MS templates, and was consistent with the hydrodynamic size measured by DLS and nanoparticle tracking analysis (Figures 1D and S2b). The thickness of air-dried AbNPs, as measured by AFM, was approximately 80 nm (Figure S4), which indicates that the assembled antibody nanoparticles were highly hydrated in aqueous solution.[27] CD spectroscopy (Figure 1E) showed that the formation of AbNPs did not affect the molecular conformation of the antibody, as the AbNPs maintained the same secondary structures as the free antibody. In addition, the AbNPs retained the main characteristic bands of the free antibody, including the amide I band at 1640 cm^{-1}, the amide II band at 1540 cm^{-1}, and amines at 3400 cm^{-1},[28] as evaluated by FTIR spectroscopy (Figure S5).

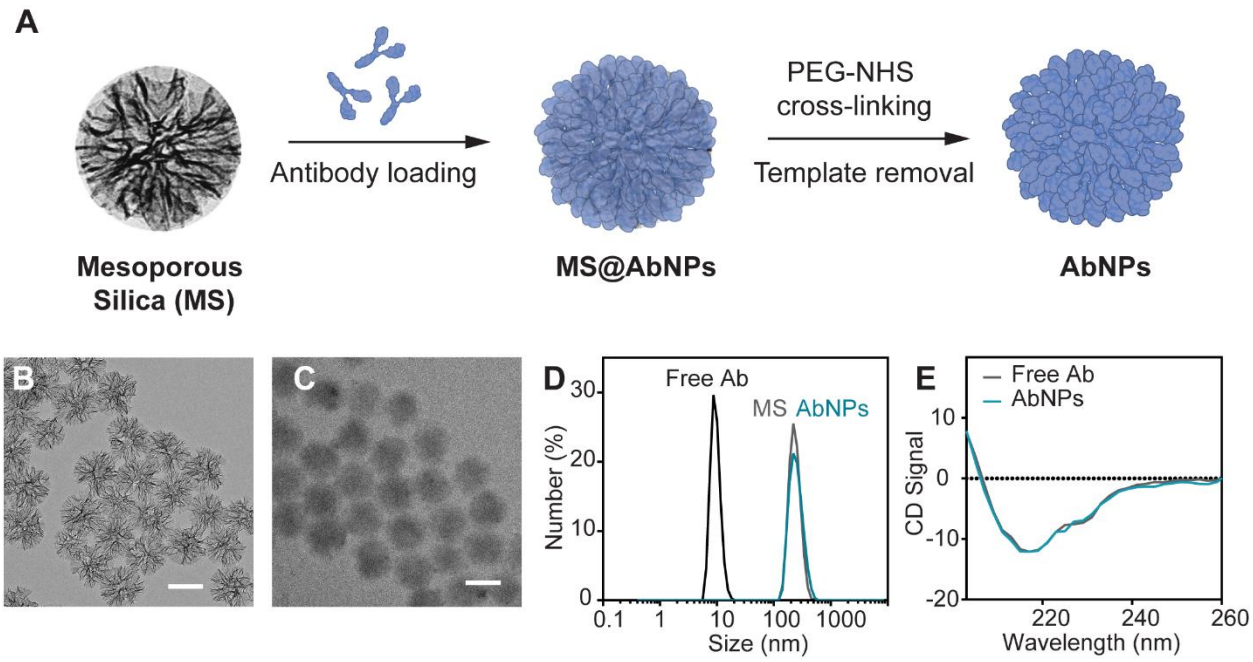

Figure 1. Preparation and characterization of AbNPs (Herceptin as model IgG molecules). (A) Schematic illustration of the template-assisted assembly of antibody molecules into AbNPs using MS as sacrificial templates. Created with BioRender.com. TEM images of (B) MS templates with large pores and (C) AbNPs after template removal; scale bars are 200 nm. (D) Size distributions of free Ab, MS templates, and AbNPs, as measured by DLS. (E) CD spectra of free Ab and AbNPs.

Binding Specificity of AbNPs. To investigate the antigen recognition ability of AbNPs, Herceptin was used as a model therapeutic IgG molecule. Herceptin, or "Trastuzumab", is an FDA-approved monoclonal antibody that targets the ErbB2 receptor, which is overexpressed in ~25% of invasive breast carcinomas.[29] The resulting AbNPs formed from Herceptin (Figures 1C, 1D, and S6) were denoted as HerNPs. HerNPs were evaluated for their ability to specifically bind to the overexpressed ErbB2 receptors in ErbB2 positive (ErbB2+) BT-474 breast cancer cells. ErbB2-negative (ErbB2−) MDA-MB-231 breast cancer cells were used as control cells (Figure 2A).

IgGNPs were used as control nanoparticles. The cell targeting ability of HerNPs mediated by ErbB2 recognition was investigated by flow cytometry and CLSM (Figures 2 and 3). Conjugation of AF488 dye to the Herceptin molecules facilitated the detection of antibodies after exposure to cells for 24 h in culture medium at 37 °C. Flow cytometry analysis revealed that the control IgGNPs had negligible binding to BT-474 cells, whereas both free Herceptin and HerNPs bound to most BT-474 cells (98% cell association) (Figure 2B). In contrast, neither the free Herceptin nor the HerNPs associated with the ErbB2− MDA-MB-231 cells (<5% nonspecific binding). To further confirm the specificity of the HerNP binding, the HER2 receptors on ErbB2+ cells were blocked by preincubating cells with free nonfluorescent Herceptin at 37 °C for 3 h. HER2 receptors are known to be rapidly recycled back to the cell surface,[30,31] and it is likely that the recycled HER2 receptors have bound Herceptin, either recycled with the receptor or from the excess Herceptin in the blocking mixture, that would sufficiently block further receptor-mediated binding of the HerNPs. Indeed, receptor blocking significantly reduced the association of HerNPs with ErbB2+ cells by over 90% (Figure 2B). These results suggest that HerNPs maintained the antigen recognition ability of Herceptin (within the nanoparticle assembly) to specifically recognize ErbB2+ cells (BT-474) by interacting with ErbB2 receptors and that binding is receptor-mediated. In addition, the results demonstrate that cross-linking Herceptin with PEG-NHS (M_w 600 g mol^{-1}) and HF treatment to remove the MS templates do not affect the recognition ability of Herceptin. Furthermore, the AF488 fluorescence intensity of the treated BT-474 cells was quantified as an indicator of the number of fluorescent antibodies associated with each cell. The fluorescence intensity of cells treated with HerNPs was higher by 45% than that of the cells treated with free Herceptin, which shows that more Herceptin is delivered to target cells when complexed into

particles (Figure 2C). This finding presents a potential strategy to achieve high antibody accumulation in target cells.

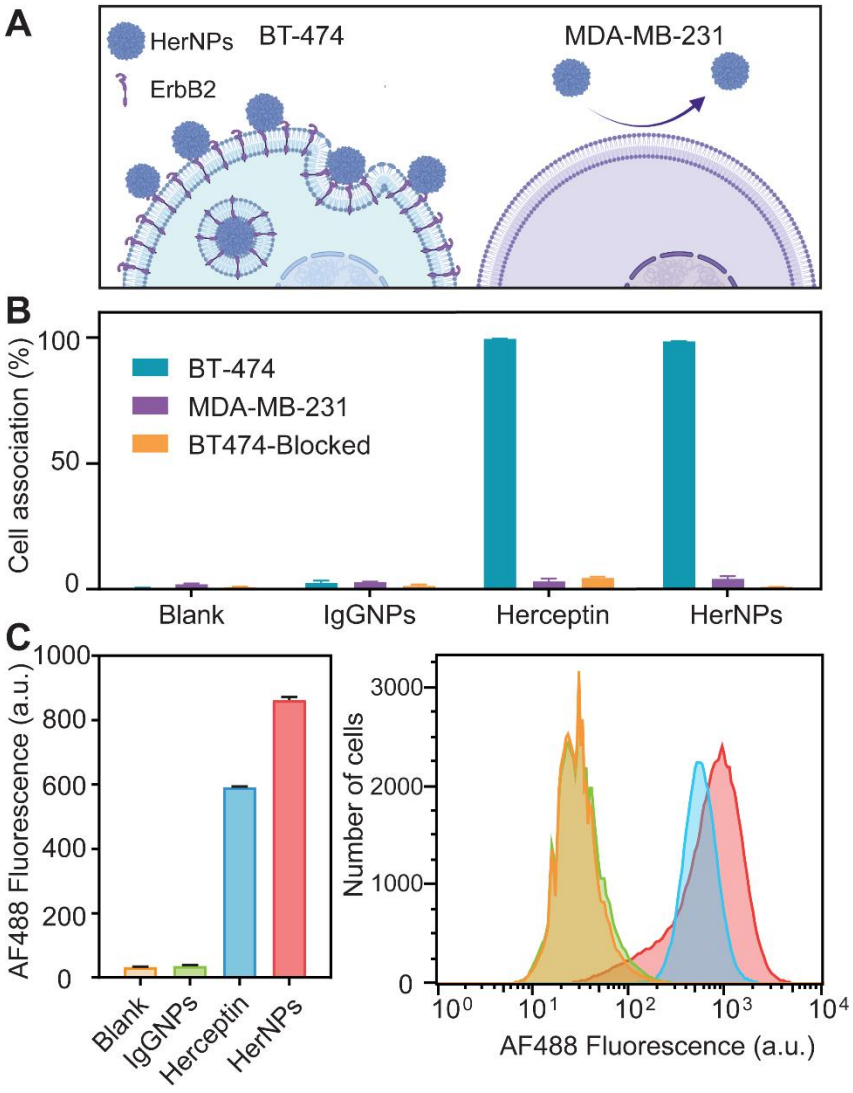

Figure 2. Selective association of HerNPs with BT-474 (ErbB2+) cells. (A) Schematic illustration of the selective cell association of HerNPs with ErbB2+ cells. Created with BioRender.com. (B) Cell association (%) profiles of HerNPs, free Herceptin, and control particles (IgGNPs) quantified by flow cytometry analysis. The free antibodies (free Herceptin) and AbNPs were labeled with AF488 and then incubated for 24 h at 37 °C with BT-474, MDA-MB-231, or ErbB2-blocked BT-474 cells. BT-474 were blocked by preincubating cells with nonfluorescent

free Herceptin (20 μg mL^{-1}) at 37 °C for 3 h to assess receptor binding specificity. The protein concentration was 20 μg mL^{-1} in all samples. (C) AF488 fluorescence intensity of BT-474 cells treated with HerNPs, free Herceptin, or control particles IgGNPs at the same protein concentration (20 μg mL^{-1}) and the corresponding flow cytometry histograms. Blank samples refer to untreated cells.

Cellular Internalization of AbNPs in Two-Dimensional (2D) and 3D Cell Models. The internalization and intracellular distribution of Herceptin and HerNPs in BT-474 cells were examined by CLSM. Following 24 h of incubation with AF488-labeled free Herceptin or HerNPs at 37 °C, BT-474 cells were washed to remove excess unbound antibody and particles, fixed and stained (nuclei) with Hoechst 33342. The ErbB2 receptors were then stained with fluorescently labeled anti-ErbB2 to visualize the antibody–receptor interactions. As observed in Figure 3A and 3B, free Herceptin colocalized with the ErbB2 receptors and was mostly distributed on the cell membrane, with limited localization in the cytoplasm at 24 h. This is consistent with previous studies that demonstrated the fast internalization and recycling of Herceptin upon binding with ErbB2 receptors on the cell membrane.[30,31] In contrast, under the same imaging conditions, the nanostructured HerNPs distributed on the cell membrane but largely accumulated in the cytoplasm with the ErbB2 receptors (Figure 3B). Cell staining with Lysotracker revealed that HerNPs were localized in the endolysosomal compartments of the BT-474 cells after internalization via receptor-mediated endocytosis (Figure S7), whereas significantly lower levels of endolysosomal colocalization was found for free Herceptin. A stronger AF488 fluorescence signal was also observed in the microscopy images of cells treated with HerNPs compared with cells treated with free Herceptin (Figure 3B), which is consistent with the mean cell fluorescence intensities determined by flow cytometry (Figure 2C). The above results suggest that HerNPs could

specifically recognize the ErbB2+ cells by interacting with the ErbB2 receptors, which is a prerequisite for the internalization of high concentrations of HerNPs via receptor-mediated endocytosis. To apply this platform to Ab with internal targets, the colocalization of the AbNPs in the endolysosomal compartments needs to be overcome, although as demonstrated in a previous study on the effect of acidic pH (pH 2.7–3.9) on antibody structure,[32] the low pH in the endosomes (pH 4.5–5.0) is not expected to adversely affect the activity of the antibody.

The internalization behavior of HerNPs was also demonstrated with a 3D tumor model comprising BT-474 cells. The spheroid tumor model was established by incubating cells in a Perfecta3D hanging drop plate in the presence of collagen. The mature spheroids (~300 μm in diameter) were treated with free Herceptin or HerNPs for 48 h at 37 °C, then visualized by membrane staining and imaged by CLSM. Cross-sectional confocal microscopy images at a depth of ~100 μm showed that both free Herceptin and HerNPs penetrated the 3D spheroids, but free Herceptin was largely localized on the cell membrane, whereas HerNPs were mostly internalized inside the cells (Figure 3C). The internalization behavior of HerNPs with the 3D model is consistent with the findings from the 2D internalization study (Figure 3B), indicating the feasibility of AbNPs to permeate solid tumor tissue.

Cytotoxicity of HerNPs. The effect of HerNPs on ErbB2+ and ErbB2− cancer cell growth was explored in vitro. As reported previously, ErbB2 signaling promotes cell proliferation and Herceptin interferes with ErbB2-triggered signaling by preventing ErbB2 receptor dimerization.[33,34] To investigate whether the cell growth inhibition function of Herceptin is preserved in HerNPs, the proliferation of ErbB2+ BT-474 and ErbB2− MDA-MB-231 cells were examined by the XTT cell viability assay after treatment with HerNPs, free Herceptin, or controls (IgGNPs) for 48 h at 37 °C. As shown in Figure 4, ~50% reduction in cell viability was observed

in BT-474 cells after treatment with HerNPs relative to the cell viability of the untreated cells (Blank), whereas no reduction in cell viability was found in MDA-MB-231 cells after treatment. Importantly, HerNPs reduced cell viability to the same extent as free Herceptin did, which suggests that HerNPs preserve the ability of free Herceptin to selectively inhibit cancer cell growth or proliferation via interaction with ErbB2 receptors.

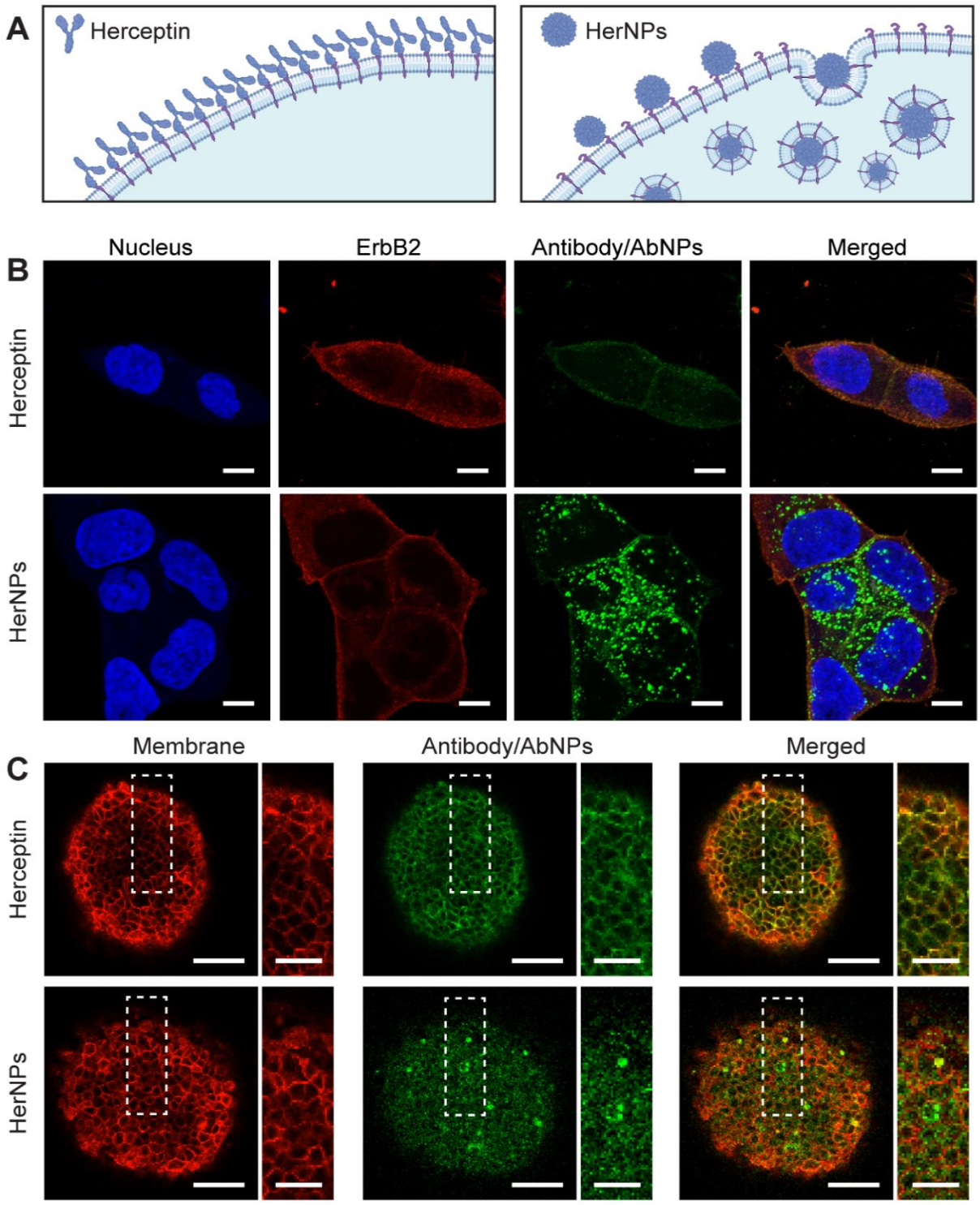

Figure 3. Cellular internalization of HerNPs in BT474 cells via ErbB2 receptor-mediated endocytosis, demonstrated on 2D and 3D models. (A) Schematic illustration of the cellular

internalization of HerNPs versus free Herceptin. Created with BioRender.com. (B) Internalization of HerNPs in BT-474 cells via ErbB2 receptor-mediated endocytosis, observed by CLSM. BT-474 cells were treated with free Herceptin or HerNPs at a dosage of 20 μg mL^{-1} for 24 h at 37 °C. Nuclei were stained with Hoechst 33342 (blue); ErbB2 receptors were immunostained with anti-ErbB2 monoclonal antibody followed by an AF594-conjugated secondary antibody (red); Herceptin antibodies were labeled with AF488 (green). Scale bars: 10 μm. (C) Internalization of HerNPs in BT-474 spheroids, observed by CLSM at a depth of ~100 μm. Mature spheroids were treated with free Herceptin or HerNPs at a dosage of 20 μg mL^{-1} for 48 h at 37 °C. Cell membranes were stained with AF594-WGA (red); Herceptin antibodies were labeled with AF488 (green). Scale bars: 100 μm. Enlarged images of regions indicated by dashed lines are shown on the right side of each image; scale bars: 50 μm.

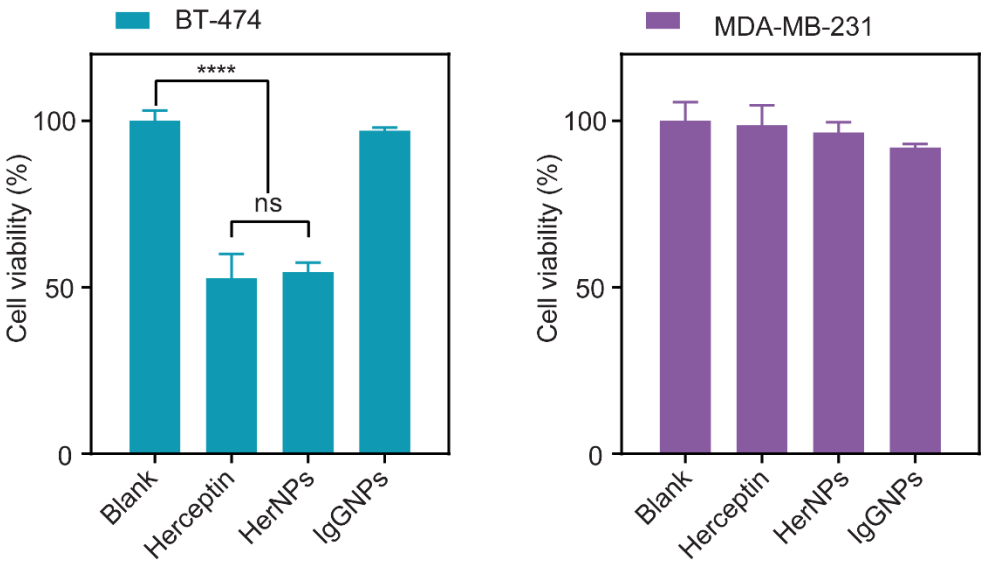

Figure 4. Cell growth inhibition effect of HerNPs on BT-474 (ErbB2+) and MDA-MB-231 (ErbB2−) cells. Cells were treated with free Herceptin, HerNPs, or IgGNPs for 48 h at 37 °C and at a protein concentration of 20 μg mL^{-1}. The cell viability was then examined by the XTT assay.

**** Indicates significant difference ($p < 0.0001$, $n = 3$); ns Indicates there is no significant difference ($p > 0.05$, $n = 3$).

Effect of the MS Core. In addition to being used as sacrificial templates in particle synthesis, MS particles are widely investigated as therapeutic delivery platforms for a range of applications.[35,36] Therefore, herein, we examined the influence of the MS core on the cell association, internalization, and cytotoxicity of the precursor particles with the MS core intact (i.e., MS@HerNPs). MS@HerNPs were less selective with regards to cell association, internalization, and cytotoxicity than the HerNPs (without MS core) (Figures S8–S10). MS@HerNPs bound to BT-474 cells (~60% cell association) but binding was to the same extent as binding to ErbB2-MDA-MB-231 cells, which indicates the non-selectivity of the binding (Figure S8). As discussed above, HerNPs showed negligible binding to MDA-MB-231 cells. No significant cytotoxicity was induced by MS@HerNPs on either cell line (Figure S10). The reduction in the targeting specificity and negligible cytotoxicity of MS@HerNPs suggest that the presence of the MS core influences receptor binding. The MS core within MS@HerNPs influences the surface properties and the mechanical property (stiffness) of the nanoparticles, possibly inducing nonspecific cellular interactions as previously observed with other MS core–polymer shell nanoparticles.[37,38] In vivo, the mechanical properties of particles have been demonstrated to affect biodistribution,[27,39,40] with softer (deformable) particles showing greater tumor accumulation and tumor penetration than stiffer particles.[39,40] This provides additional motivation for MS core removal for in vivo tumor targeting applications. In addition, in MS@HerNPs, the antibodies could also be buried within the pores of the core, hindering their ability to bind to their target receptors on cell membranes. In addition, differences in the biomolecular corona formed on MS@HerNPs and HerNPs may influence targeting specificity (biomolecular corona formation is affected by several factors,

including the physichochemical properties of the particles, types of targeting ligands, as well as the biological environment).[41–43]

Assembly of an Antibody–Drug Conjugate. After demonstrating the selectivity and uptake of HerNPs via receptor-mediated endocytosis, a Herceptin–drug conjugate, Kadcyla, was applied to demonstrate the versatility of the AbNP platform. Kadcyla (also known as ado-trastuzumab emtansine) was approved by the FDA in 2019 as an antibody–drug conjugate for clinical ErbB2+ breast cancer treatment.[44] It is composed of the ErbB2 receptor targeting monoclonal antibody, Herceptin (trastuzumab), and a cytotoxic agent emtansine (DM1) that inhibits microtubule polymerization to cause cell-cycle arrest and cell death.[45,46] Upon binding to subdomain IV of the ErbB2 receptor, Kadcyla undergoes receptor-mediated internalization and lysosomal degradation, resulting in the intracellular release of DM1.[47] KadNPs were prepared via the template-assisted antibody assembly method as described for HerNPs (Figures S11 and S12). The selective cell association of KadNPs was evaluated on ErbB2+ BT-474 cells and ErbB2− MDA-MB-231 by flow cytometry. As observed in Figure 5B, KadNPs maintained the targeting ability of free Kadcyla to selectively associate with ErbB2+ BT-474 cells. To assess whether the intracellular effect of Kadcyla is enhanced, cellular internalization was investigated using CLSM, and the cell growth inhibition was examined. The results showed that KadNPs were largely internalized inside the target cells, whereas free Kadcyla appeared mostly distributed on the membrane (Figure 5C), potentially after receptor recycling. Moreover, KadNPs exhibited higher cytotoxicity in BT-474 cells than free Kadcyla (Figure 5D), likely owing to the enhanced internalization and accumulation of DM1 inside the cells (Figure 5A). Under the same incubation conditions, KadNPs appeared more cytotoxic than HerNPs (Figures 4, 5D, and S13). Overall, the ability to assemble antibody–drug conjugates, such as Kadcyla, into homogeneous particles and enhance the concentration of

the conjugated drug intracellularly holds promise for the codelivery of cargo with internal targets combined with the cell surface specificity that can be afforded with a receptor-targeted antibody. Indeed, we investigated whether AbNPs could be assembled using a reducible disulfide-containing PEG cross-linker (Figure S14). Using gel electrophoresis, the particles disassembled into their antibody building blocks in the presence of physiological levels of glutathione (5 mM), which paves way for investigating the assembly of antibodies with intracellular targets.

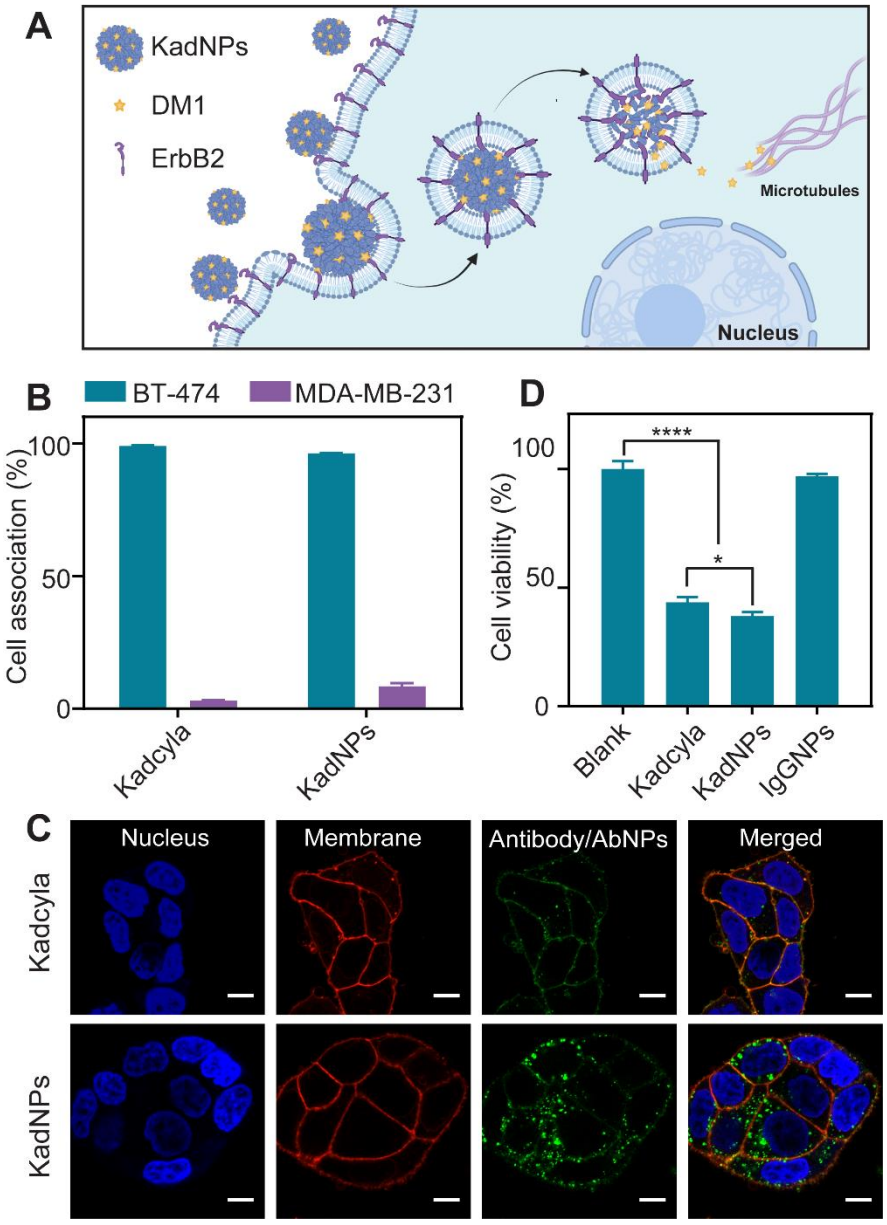

Figure 5. Bioactivity of KadNPs: Cell association, internalization, and growth inhibition. (A) Schematic illustration of the interactions between KadNPs and cells. KadNPs selectively bind to the ErbB2 receptor on the cell membrane and are internalized via ErbB2-mediated endocytosis. Lysosomal degradation results in the release of DM1 into the cytoplasm causing cell-cycle arrest and cell death. Created with BioRender.com. (B) Flow cytometry analysis showing the association of KadNPs and free Kadcyla with BT-474 (ErbB2+) and MDA-MB-231 (ErbB2−) cells after 24 h incubation at 37 °C. (C) Internalization of KadNPs in BT-474 cells after 24 h treatment at 37 °C, as observed by CLSM. Nuclei were stained with Hoechst 33342 dye (blue); Cell membranes were stained with AF594-WGA (red); Kadcyla antibodies were labeled with AF488 (green). Scale bars: 10 μm. (D) Viability of cells, assessed by XTT assay, after treatment with free Kadcyla, KadNPs, or IgGNPs for 48 h at 37 °C at a protein concentration of 20 μg mL^{-1}. **** Indicates significant difference ($p < 0.0001$, $n = 3$); * Indicates significant difference ($p < 0.05$, $n = 3$).

Biodistribution and Tumor Accumulation. The behavior of the AbNPs in comparison with free antibody was assessed in vivo (Figure 6). Using Herceptin as the model antibody, Tm-labeled free Herceptin and HerNPs were prepared using a macrocyclic bifunctional chelator (*p*-SCN-Bn-DOTA). The organ-level biodistribution of free Herceptin and HerNPs at 4 h post-administration in BALB/c mice was qualitatively determined using ICP-MS on digested tissue preparations. As shown in Figure 6, the HerNPs had pronounced uptake in the spleen and liver, where small amounts of free antibody were detected. The low level of HerNPs in the blood also indicates that at 4 h, most of the particles are cleared, whereas free antibody remained in the circulation. Nevertheless, this shows that in future studies, antibodies with potential targets in the liver and spleen may be used in the assembly. While it is likely that most particles are being sequestered by macrophages in the liver and spleen, the particles may also access the space of Disse via the

sinusoidal fenestrations to reach hepatic stellate cells, which are principal players in liver fibrosis that can lead to liver cirrhosis and liver cancer. Several monoclonal antibodies, for example, are being investigated against liver fibrosis, including anti-connective tissue growth factor (CTGF)[48] and anti-lysyl oxidase-like 2 (LOXL2).[49] There are also monoclonal antibodies that target hepatic tumor cells including atezolizumab[50] (FDA-approved to treat liver cancer) that may be assembled into particles.

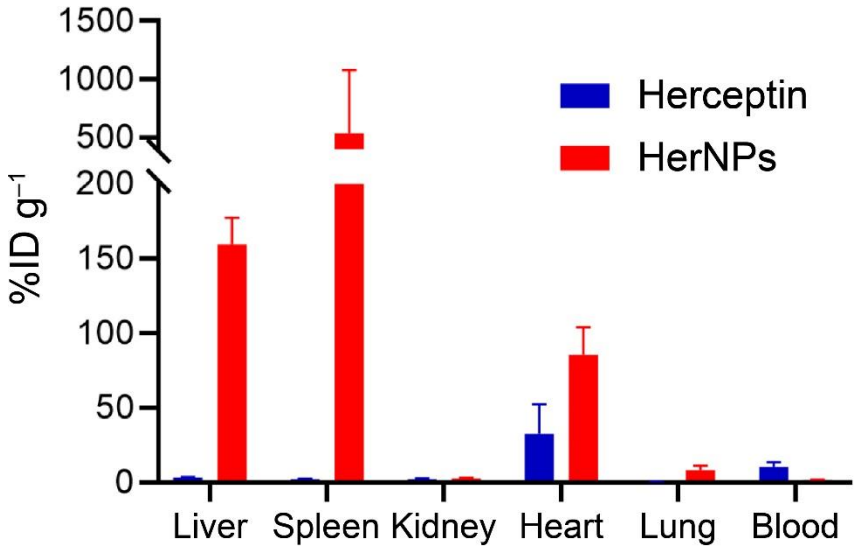

Figure 6. In vivo biodistribution of Tm-labeled free Herceptin and HerNPs at 4 h post-injection in healthy BALB/c mice. The data are reported as a percentage of injected dose per gram of tissue (%ID g^{-1}) and presented as means ± standard deviations based on triplicate samples.

Free Herceptin and HerNPs were also assessed for their capacity to target tumors (Figure S15). ^{89}Zr-labeled free Herceptin and HerNPs were prepared using a DFO chelator and injected in BALB/c mice bearing subcutaneous BT-474 tumors at a dosage of 2.0 MBq for each sample. ^{89}Zr-labeled free IgG and IgGNPs were also prepared and injected at the same dosage as controls. The biodistribution of the free antibodies and particles at 5 days post-administration was determined by PET-CT imaging of tumor-bearing mice (whole animal imaging and harvested organs/tissues

at day 5). Low bone uptake suggests that the PET-CT imaging isotope ^{89}Zr remained chelated to the particle during the study. As shown in Figure S15, there was no accumulation of HerNPs in the BT-474 tumors in vivo, whereas the binding of free Herceptin to tumors remained high after 5 days. At 4 h post-administration, bladder accumulation was minimal (Figure S16), which indicates that the particles remained intact in vivo and did not instantaneously dissemble into smaller fragments that can be filtered out by the kidneys. Liver accumulation was also observed for the HerNPs and IgGNPs in tumor-bearing mice after 4 h (Figure S16), which is consistent with the ICP-MS data obtained from healthy mice (Figure 6), although liver accumulation decreased from ~25% ID g^{-1} to ~20% ID g^{-1} from 4 h to 5 days, suggesting the potential for particle clearance over time. These results suggest that further engineering of the AbNPs is needed for their application in tumor-targeting outside the liver and spleen. Engineering the size and the PEG density of the AbNPs may be means to reduce immune recognition and improve their tumor targeting capacity in vivo. Nonetheless, with the wide applicability of monoclonal antibodies as shown in a schematic in Figure S17, the assembly of Abs into controlled NPs could lead to targeted multifunctional particle-based Ab depots for a range of applications.

CONCLUSIONS

This study demonstrates a versatile template-assisted antibody assembly platform that offers wide applicability to a range of therapeutic antibodies and antibody–drug conjugates. The AbNPs prepared by the assembly method exhibited well-defined size and morphology and retained the antigen or receptor binding specificity of the free antibody. Importantly, the particulate nature of the AbNPs afforded increased antibody internalization and accumulation and enhanced subsequent intracellular responses such as cell growth inhibition. These findings provide evidence that AbNPs can mediate cell processes that are different to those of free antibodies. The template-assisted

assembly of antibodies provides a platform for exploring and understanding the biological behavior of well-defined antibody nanostructures and can facilitate the engineering of combinatorial and multifunctional antibody assemblies for use as therapeutic agents and in diagnostics. Our future work is focused on examining the effect of antibody nanoparticle engineering on their in vivo behavior, including immunogenicity, targeting ability, and therapeutic efficacy.

ASSOCIATED CONTENT

Supporting Information. N_2 adsorption–desorption isotherm and pore size distributions of the MS templates; particle concentration and size distribution of MS templates and AbNPs using nanoparticle tracking analysis; loading capacity of lysozyme, BSA, and IgG in MS templates; AFM analysis of IgGNPs; FTIR spectra of free IgG and IgGNPs; zeta potential profile of free Herceptin and Kadcyla, MS, HerNPs, and KadNPs; colocalization of free Herceptin and HerNPs with lysosomal compartments of BT-474 cells; association of MS@HerNPs with BT-474 and MDA-MB-231 cells; internalization of MS@HerNPs in BT-474 cells by confocal microscopy; viability of cells treated with MS@HerNPs; TEM and size distribution of KadNPs; viability of cells treated with free Kadcyla and KadNPs; and MIRIBEL checklist for reporting research in bio–nano science. This material is available free of charge *via* the Internet at http://pubs.acs.org.

AUTHOR INFORMATION

Corresponding author

*E-mail: fcaruso@unimelb.edu.au

Notes

The authors declare no competing financial interests.

ACKNOWLEDGMENT

This research was conducted and funded by the Australian Research Council Centre of Excellence in Convergent Bio-Nano Science and Technology (project number CE140100036). C.E.H and F.C. acknowledge the award of a National Health and Medical Research Council (NHMRC) Project Grant (GNT1138361) that also supported this work. F.C. acknowledges the award of an NHMRC Senior Principal Research Fellowship (GNT1135806). This work received funding from the European Union's Horizon 2020 research and innovation program under the Marie Skłodowska-Curie grant agreement no. 690901 ("NANOSUPREMI"). This work was performed in part at the Materials Characterisation and Fabrication Platform (MCFP) at The University of Melbourne and the Victorian Node of the Australian National Fabrication Facility (ANFF). We thank Dr Andrew Mitchell (MCFP) for his valuable contribution in obtaining ethics approval.

REFERENCES

(1) Back, M.; Hansson, G. K. Anti-inflammatory Therapies for Atherosclerosis. *Nat. Rev. Cardiol.* **2015**, *12*, 199–211.

(2) Beck, A.; Wurch, T.; Bailly, C.; Corvaia, N. Strategies and Challenges for the Next Generation of Therapeutic Antibodies. *Nat. Rev. Immunol.* **2010**, *10*, 345–352.

(3) Thomas, A.; Teicher, B. A.; Hassan, R. Antibody–Drug Conjugates for Cancer Therapy. *Lancet Oncol.* **2016**, *17*, e254–e262.

(4) Bournazos, S.; Wang, T. T.; Dahan, R.; Maamary, J.; Ravetch, J. V. Signaling by Antibodies: Recent Progress. *Annu. Rev. Immunol.* **2017**, *35*, 285–311.

(5) Trenevska, I.; Li, D.; Banham, A. H. Therapeutic Antibodies against Intracellular Tumor Antigens. *Front. Immunol.* **2017**, *8*, 1001.

(6) Beck, A.; Goetsch, L.; Dumontet, C.; Corvaia, N. Strategies and Challenges for the Next Generation of Antibody Drug Conjugates. *Nat. Rev. Drug Discovery* **2017**, *16*, 315–337.

(7) Torchilin, V. P. Recent Advances with Liposomes as Pharmaceutical Carriers. *Nat. Rev. Drug Discovery* **2005**, *4*, 145–160.

(8) Lohcharoenkal, W.; Wang, L.; Chen, Y. C.; Rojanasakul, Y. Protein Nanoparticles as Drug Delivery Carriers for Cancer Therapy. *Biomed. Res. Int.* **2014**, *2014*, 180549.

(9) Amjad, M. W.; Kesharwani, P.; Amin, M. C. I. M.; Iyer, A. K. Recent Advances in the Design, Development, and Targeting Mechanisms of Polymeric Micelles for Delivery of siRNA in Cancer Therapy. *Prog. Polym. Sci.* **2017**, *64*, 154–181.

(10) Jiang, W.; Kim, B. Y. S.; Rutka, J. T.; Chan, W. C. W. Nanoparticle-Mediated Cellular Response is Size-Dependent. *Nat. Nanotechnol.* **2008**, *3*, 145–150.

(11) Kolhar, P.; Anselmo, A. C.; Gupta, V.; Pant, K.; Prabhakarpandian, B.; Ruoslahti, E.; Mitragotri, S. Using Shape Effects to Target Antibody-Coated Nanoparticles to Lung and Brain Endothelium. *Proc. Natl. Acad. Sci. U. S. A.* **2013**, *110*, 10753–10758.

(12) Barua, S.; Yoo, J. W.; Kolhar, P.; Wakankar, A.; Gokarn, Y. R.; Mitragotri, S. Particle Shape Enhances Specificity of Antibody-Displaying Nanoparticles. *Proc. Natl. Acad. Sci. U. S. A.* **2013**, *110*, 3270–3275.

(13) Zhang, S.; Li, J.; Lykotrafitis, G.; Bao, G.; Suresh, S. Size-Dependent Endocytosis of Nanoparticles. *Adv. Mater.* **2009**, *21*, 419–424.

(14) Cui, J.; Ju, Y.; Houston, Z. H.; Glass, J. J.; Fletcher, N. L.; Alcantara, S.; Dai, Q.; Howard, C. B.; Mahler, S. M.; Wheatley, A. K. et al. Modulating Targeting of Poly(ethylene glycol) Particles to Tumor Cells Using Bispecific Antibodies. *Adv. Healthcare Mater.* **2019**, *8*, e1801607.

(15) Dong, X. H.; Obermeyer, A. C.; Olsen, B. D. Three-Dimensional Ordered Antibody Arrays Through Self-Assembly of Antibody–Polymer Conjugates. *Angew. Chem. Int. Ed.* **2017**, *56*, 1273–1277.

(16) Chung, J. E.; Tan, S.; Gao, S. J.; Yongvongsoontorn, N.; Kim, S. H.; Lee, J. H.; Choi, H. S.; Yano, H.; Zhuo, L.; Kurisawa, M.; et al. Self-Assembled Micellar Nanocomplexes Comprising Green Tea Catechin Derivatives and Protein Drugs for Cancer Therapy. *Nat. Nanotechnol.* **2014**, *9*, 907–912.

(17) Cromwell, M. E. M.; Hilario, E.; Jacobson, F. Protein Aggregation and Bioprocessing. *AAPS J.* **2006**, *8*, E572–E579.

(18) Joubert, M. K.; Luo, Q. Z.; Nashed-Samuel, Y.; Wypych, J.; Narhi, L. O. Classification and Characterization of Therapeutic Antibody Aggregates. *J. Biol. Chem.* **2011**, *286*, 25118–25133.

(19) Gause, K. T.; Yan, Y.; Cui, J.; O'Brien-Simpson, N. M.; Lenzo, J. C.; Reynolds, E. C.; Caruso, F. Physicochemical and Immunological Assessment of Engineered Pure Protein Particles with Different Redox States. *ACS Nano* **2015**, *9*, 2433–2444.

(20) Yang, Y. N.; Bernardi, S.; Song, H.; Zhang, J.; Yu, M. H.; Reid, J. C.; Strounina, E.; Searles, D. J.; Yu, C. Z. Anion Assisted Synthesis of Large Pore Hollow Dendritic Mesoporous Organosilica Nanoparticles: Understanding the Composition Gradient. *Chem. Mater.* **2016**, *28*, 704–707.

(21) Kwon, D.; Cha, B. G.; Cho, Y.; Min, J.; Park, E. B.; Kang, S. J.; Kim, J. Extra-Large Pore Mesoporous Silica Nanoparticles for Directing in Vivo M2 Macrophage Polarization by Delivering IL-4. *Nano Lett.* **2017**, *17*, 2747–2756.

(22) Chiu, H. Y.; Goss, D.; Haddick, L.; Engelke, H.; Bein, T. Clickable Multifunctional Large-Pore Mesoporous Silica Nanoparticles as Nanocarriers. *Chem. Mater.* **2018**, *30*, 644–654.

(23) Bjornmalm, M.; Faria, M.; Chen, X.; Cui, J.; Caruso, F. Dynamic Flow Impacts Cell–Particle Interactions: Sedimentation and Particle Shape Effects. *Langmuir* **2016**, *32*, 10995–11001.

(24) Faria, M.; Björnmalm, M.; Thurecht, K. J.; Kent, S. J.; Parton, R. G.; Kavallaris, M.; Johnston, A. P.; Gooding, J. J.; Corrie, S. R.; Boyd, B. J. et al. Minimum Information Reporting in Bio–Nano Experimental Literature. *Nat. Nanotechnol.* **2018**, *13*, 777–785.

(25) Tan, Y. H.; Liu, M.; Nolting, B.; Go, J.G.; Gervay-Hague, J; Liu, G.Y. A Nanoengineering Approach for Investigation and Regulation of Protein Immobilization. *ACS Nano* **2008**, *2*, 2374-2384.

(26) Ejima, D.; Tsumoto, K.; Fukada, H.; Yumioka, R.; Nagase, K.; Arakawa, T.; Philo, J. S. Effects of Acid Exposure on the Conformation, Stability, and Aggregation of Monoclonal Antibodies. *Proteins* **2007**, *66*, 954–962.

(27) Cui, J. W.; De Rose, R.; Alt, K.; Alcantara, S.; Paterson, B. M.; Liang, K.; Hu, M.; Richardson, J. J.; Yan, Y.; Jeffery, C. M. et al. Engineering Poly(ethylene glycol) Particles for Improved Biodistribution. *ACS Nano* **2015**, *9*, 1571–1580.

(28) Manning, M. C. Use of Infrared Spectroscopy to Monitor Protein Structure and Stability. *Expert Rev. Proteomics* **2005**, *2*, 731–743.

(29) Slamon, D. J.; Godolphin, W.; Jones, L. A.; Holt, J. A.; Wong, S. G.; Keith, D. E.; Levin, W. J.; Stuart, S. G.; Udove, J.; Ullrich, A. et al. Studies of the HER-2/Neu Proto-Oncogene in Human Breast and Ovarian Cancer. *Science* **1989**, *244*, 707–712.

(30) Austin, C. D.; De Maziere, A. M.; Pisacane, P. I.; van Dijk, S. M.; Eigenbrot, C.; Sliwkowski, M. X.; Klumperman, J.; Scheller, R. H. Endocytosis and Sorting of ErbB2 and the Site of Action of Cancer Therapeutics Trastuzumab and Geldanamycin. *Mol. Biol. Cell* **2004**, *15*, 5268–5282.

(31) Bertelsen, V.; Stang, E. The Mysterious Ways of ErbB2/HER2 Trafficking. *Membranes* **2014**, *4*, 424–446.

(32) Ejima, D.; Tsumoto, K.; Fukada, H.; Yumioka, R.; Nagase, K.; Arakawa, T.; Philo, J. S. Effects of Acid Exposure on the Conformation, Stability, and Aggregation of Monoclonal Antibodies, *Proteins* **2007**, *66*, 954–962.

(33) Hudis, C. A. Trastuzumab—Mechanism of Action and Use in Clinical Practice. *N. Engl. J. Med.* **2007**, *357*, 39–51.

(34) Arteaga, C. L.; Sliwkowski, M. X.; Osborne, C. K.; Perez, E. A.; Puglisi, F.; Gianni, L. Treatment of HER2-Positive Breast Cancer: Current Status and Future Perspectives. *Nat. Rev. Clin. Oncol.* **2011**, *9*, 16–32.

(35) Manzano, M.; Vallet-Regí, M. Mesoporous Silica Nanoparticles for Drug Delivery. *Adv. Funct. Mater.* **2020**, *30*,1902634.

(36) Xu, C.; Lei, C; Yu, C. Mesoporous Silica Nanoparticles for Protein Protection and Delivery. *Front. Chem.* **2019**, *7*, 290.

(37) Ju, Y.; Kelly, H. G.; Dagley, L. F.; Reynaldi, A.; Schlub, T. E.; Spall, S. K.; Bell, C. A.; Cui, J.; Mitchell, A. J.; Lin, Z. et al. Person-Specific Biomolecular Coronas Modulate Nanoparticle Interactions with Immune Cells in Human Blood. *ACS Nano* **2020**, *14*, 15723–15737.

(38) Song, J.; Ju, Y.; Amarasena, T. H.; Lin, Z.; Mettu, S.; Zhou, J.; Rahim, M. A.; Ang, C.-S.; Cortez-Jugo, C.; Kent, S. J. et al. Influence of Poly(ethylene glycol) Molecular Architecture on Particle Assembly and Ex Vivo Particle–Immune Cell Interactions in Human Blood. *ACS Nano* **2021**, *15*, 10025–10038.

(39) Guo, P.; Liu, D.; Subramanyam, K.; Wang, B.; Yang, J.; Huang, J.; Auguste, D. T.; Moses, M. A. Nanoparticle Elasticity Directs Tumor Uptake. *Nat. Commun.* **2018**, *9*, 130.

(40) Liang, Q.; Bie, N.; Yong, T.; Tang, K.; Shi, X.; Wei, Z.; Jia, H.; Zhang, X.; Zhao, H.; Huang, W. et al. The Softness of Tumour-Cell-Derived Microparticles Regulates Their Drug-Delivery Efficiency. *Nat. Biomed. Eng.* **2019**, *3*, 729–740.

(41) Dai, Q.; Yan, Y.; Ang, C.-S.; Kempe, K.; Kamphuis, M. M.; Dodds, S. J.; Caruso, F. Monoclonal Antibody-Functionalized Multilayered Particles: Targeting Cancer Cells in the Presence of Protein Coronas. *ACS Nano* **2015**, *9*, 2876–2885.

(42) Salvati, A.; Pitek, A. S.; Monopoli, M. P.; Prapainop, K.; Bombelli, F. B.; Hristov, D. R.; Kelly, P. M.; Aberg, C.; Mahon, E.; Dawson, K. A. Transferrin-Functionalized Nanoparticles Lose Their Targeting Capabilities when a Biomolecule Corona Adsorbs on the Surface. *Nat. Nanotechnol.* **2013**, *8*, 137–143.

(43) Ju, Y.; Dai, Q.; Cui, J.; Dai, Y.; Suma, T.; Richardson, J. J.; Caruso, F. Improving Targeting of Metal–Phenolic Capsules by the Presence of Protein Coronas. *ACS Appl. Mater. Interfaces* **2016**, *8*, 22914–22922.

(44) Chau, C. H.; Steeg, P. S.; Figg, W. D. Antibody–Drug Conjugates for Cancer. *Lancet* **2019**, *394*, 793–804.

(45) von Minckwitz, G.; Huang, C. S.; Mano, M. S.; Loibl, S.; Mamounas, E. P.; Untch, M.; Wolmark, N.; Rastogi, P.; Schneeweiss, A.; Redondo, A. et al. Trastuzumab Emtansine for Residual Invasive HER2-Positive Breast Cancer. *N. Engl. J. Med.* **2019**, *380*, 617–628.

(46) Lewis Phillips, G. D.; Li, G.; Dugger, D. L.; Crocker, L. M.; Parsons, K. L.; Mai, E.; Blattler, W. A.; Lambert, J. M.; Chari, R. V.; Lutz, R. J. et al. Targeting HER2-Positive Breast Cancer with Trastuzumab-DM1, an Antibody-Cytotoxic Drug Conjugate. *Cancer Res.* **2008**, *68*, 9280–9290.

(47) Junttila, T. T.; Li, G.; Parsons, K.; Phillips, G. L.; Sliwkowski, M. X. Trastuzumab-DM1 (T-DM1) Retains all the Mechanisms of Action of Trastuzumab and Efficiently Inhibits Growth of Lapatinib Insensitive Breast Cancer. *Breast Cancer Res. Treat.* **2011**, *128*, 347–356.

(48) Lipson, K. E.; Wong, C.; Teng, Y.; Spong, S. CTGF Is a Central Mediator of Tissue Remodeling and Fibrosis and Its Inhibition Can Reverse the Process of Fibrosis. *Fibrog. Tissue Repair* **2012**, *5*, S24.

(49) Ikenaga, N.; Peng, Z. W.; Vaid, K. A.; Liu, S. B.; Yoshida, S.; Sverdlov, D. Y.; Mikels-Vigdal, A.; Smith, V.; Schuppan, D; Popov, Y. V. Selective Targeting of Lysyl Oxidase-Like 2

(LOXL2) Suppresses Hepatic Fibrosis Progression and Accelerates Its Reversal. *Gut* **2017**, *66*, 1697–1708.

(50) Finn, R. S.; Qin, S.; Ikeda, M.; Galle, P. R.; Ducreux, M.; Kim, T. Y.; Kudo, M.; Breder, V.; Merle, P.; Kaseb, A. O. et al. Atezolizumab Plus Bevacizumab in Unresectable Hepatocellular Carcinoma. *N. Engl. J. Med.* **2020**, *382*, 1894–1905.

Table of Contents Graphic